Journal of Materials Chemistry A

Accepted Manuscript

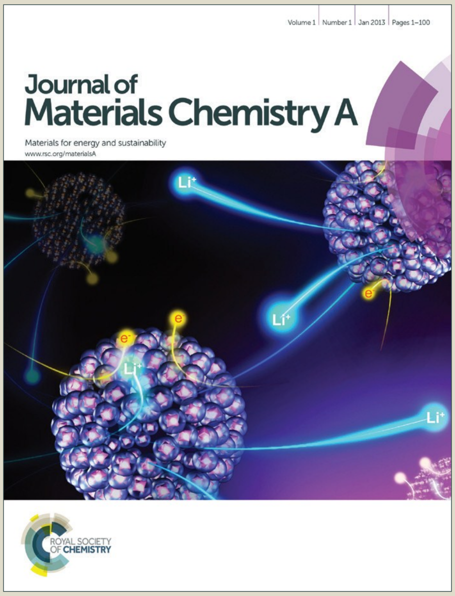

ROYAL SOCIETY OF CHEMISTRY

www.rsc.org/materialsA

Journal Name

ARTICLE

Bi-layer lithium phosphorous oxynitride/aluminium substituted lithium lanthanum titanate as promising solid electrolyte for long-life rechargeable lithium-oxygen batteries

Received 00th January 20xx,
Accepted 00th January 20xx

DOI: 10.1039/x0xx00000x

www.rsc.org/

Hang T.T. Le, Ramchandra S. Kalubarme, Duc Tung Ngo, Harsharaj S. Jadhav, and Chan- Jin Park*

Lithium ion conducting membranes are indispensable for building lithium-air (oxygen) batteries employing aqueous and non-aqueous electrolytes for long-term operation. In this report, we present the high performance of a non-aqueous lithium–air batteries, in which a bilayer lithium phosphorous oxynitride/aluminium substituted lithium lanthanum titanate solid electrolyte is employed as a protective layer for a lithium metal electrode and free carbon-manganese dioxide as the cathodic catalyst. Aluminium-doped lithium lanthanum titanate (A-LLTO) pellets were prepared using citrate-gel synthesis followed by pelletization and sintering process. A thin lithium phosphorous oxynitride (LiPON) layer was then deposited on the A-LLTO using the sputtering method, which was used as a protective interlayer for separating A-LLTO ceramic from a Li metal electrode. With the high ionic conductivity of 2.25×10^{-4} S cm^{-1} and large electrochemical stability window of 0-5 V, the LiPON/A-LLTO ceramics showed promising feasibility as a stable solid electrolyte for application in Li-O_2 batteries. The aprotic Li-O_2 cell containing the Li metal electrode protected by LiPON/A-LLTO exhibited excellent charge-discharge cycling stability with a long life span of 128 cycles under the limited capacity mode of 1000 mA h g^{-1}. After the cycling test, the LiPON/A-LLTO ceramics retained high ion conductivity of 1.65×10^{-4} S cm^{-1}. In addition, with the introduction of LiPON/A-LLTO, the Li dendrite growth and electrolyte decomposition are effectively suppressed.

Introduction

Recently, lithium-air (lithium-oxygen) batteries have received considerable worldwide attention due to their outstanding energy densities.[1-4] Two main types of lithium-air (Li-air) battery systems employing aprotic and aqueous electrolytes, which have the theoretical energy densities of 3456 Wh kg^{-1} and 2450 Wh kg^{-1} (including oxygen), respectively, have been studied previously. Use of the aqueous system avoids the issue of cathode clogging because the reaction products are water soluble.[5] However, lithium metal reacts violently with water, and thus a solid electrolyte layer is certainly indispensable.

Compared with the aqueous system, the aprotic system has a ~30% larger energy density. Nevertheless, this system has suffers from several issues, such as electrolyte consumption during charging due to the attack of oxygen radicals. Recent works on aprotic type batteries have reported the acceptable stability and cycling performance of batteries utilizing long chain, ether-based glyme solvents such as tetraethylene glycol dimethyl ether (TEGDME).[6-10] Regarding lithium electrode, due to the highly reactive nature of lithium electrode, during the charge/discharge process of aprotic cells, a solid electrolyte interphase (SEI) layer forms on its surface via the unexpected electrolyte decomposition and/or reaction between Li metal and supplied gases. In particular, the non-uniform chemical composition of the SEI layer can induce an uneven current distribution on the electrode surface, which is responsible for the growth of Li dendrites and the eventual electric short caused by the direct contact between the anode and cathode.[11-13] This problem can be addressed by sandwiching a Li-ion conducting solid electrolyte between the Li metal and the air electrode with the following aims. (i) Preventing the Li metal from reacting with poisonous species such as water, O_2, and CO_2 diffused from the cathode side to the anode side, thereby leading to a significant increase in the lifetime of the battery and (ii) suppressing the initiation and growth of Li dendrite, which eventually alleviates the reductive decomposition of the electrolyte and safety concerns.[14]

To date, various solid electrolyte materials including polymer/polymer-ceramic composites, non-oxide inorganic compounds, single-crystalline silicon, and oxides such as perovskite-type oxides, garnet-type oxides, γ-Li_3PO_4 oxides, and Na super ionic conductor (NASICON) analogue-type oxides with good Li-ion conductivity have been comprehensively studied.[15-20] Nevertheless, only a few of the NASICON-type oxides and single-crystalline silicon have been evaluated as lithium ion conducting membranes in lithium-air battery cells. Moreover, the use of these inorganic solid electrolytes has often been considered thus far for aqueous or hybrid (aqueous + non-aqueous) electrolyte based batteries,[5, 21-27] where the

---

Department of Materials Science and Engineering, Chonnam National University, 77, Yongbongro, Bukgu, Gwangju 500-757, South Korea
**E-mail: parkcj@jnu.ac.kr*

†Electronic Supplementary Information (ESI) available: See DOI: 10.1039/x0xx00000x

NASICON-type oxides such as lithium aluminium titanium phosphate (LATP) have been used as a separator to protect Li metal against water. Other solid electrolytes still show promising development as lithium ion conducting membranes for lithium-air batteries.

Since Inaguma et al. reported the first study on the ionic conductivity of lithium-lanthanum titanate (LLTO) ceramic with a bulk Li-ion conductivity of up to 1×10^{-3} S cm^{-1} at room temperature,[28] LLTO has attracted worldwide interest due to its high potential as a solid electrolyte in various electrochemical devices including Li-air batteries. Specifically, the LLTO has a high bulk conductivity for Li-ion at room temperature (~10^{-3} S cm^{-1}),[16, 28] a high Li-ion diffusion coefficient (10^{-6}-10^{-7} cm^2 s^{-1}),[28, 29] a low electronic conductivity (from 5×10^{-10} to 1×10^{-8} S cm^{-1}),[28, 30, 31] a large electrochemical window (greater than 4 V),[31, 32] and a high thermal stability from 4 K to 1600 K without any phase transition.[32] However, the insufficient total conductivity due to large grain boundary resistance and the difficulty in controlling Li content in LLTO and Li-ion conductivity (especially after high temperature annealing) are remaining issues that should be addressed. Furthermore, when the LLTO makes direct contact with the Li metal, Ti^{4+} in LLTO can be reduced to Ti^{3+} by metallic Li, leading to an increase in the electronic conductivity of LLTO.[33] Until now, few groups have succeeded in gaining a total conductivity of greater than 1×10^{-4} S cm^{-1}.[34, 35] Accordingly, the use of LLTO as a solid electrolyte is still limited. In particular, the application of LLTO solid electrolyte in aprotic type Li-air batteries (where the protection of the Li electrode against impurity gases and the growth of Li dendrite appears to be needed), has rarely been reported.

Recently, we reported the improvement in the total ionic conductivity of LLTO ceramics, originally fabricated based on the citrate gel method, through the partial substitution of Ti by Al and the addition of excess Li_2O.[36] The developed LLTO was referred as A-LLTO. In this study, we additionally deposited a lithium phosphorous oxynitride (LiPON) interlayer on the A-LLTO (LiPON/A-LLTO) using the radio frequency (RF)-sputtering method to prevent the direct contact between Li metal and A-LLTO. Further, the electrochemical performance of lithium-oxygen (Li-O_2) cells employing the LiPON/A-LLTO solid electrolytes and the carbon-free oxygen electrode were investigated.

Experimental

Preparation of LiPON/A-LLTO pellets: A-LLTO powder with the nominal composition of $(Li_{0.33}La_{0.56})_{1.005}Ti_{0.99}Al_{0.01}O_3$ was prepared via the citrate-gel method from $LiNO_3$, $La(NO_3)_3.6H_2O$, $Al(NO_3)_3.9H_2O$, titanium isopropoxide, ethylene glycol, and citric acid, as well as an excess amount of $LiNO_3$ of 20 mol.% to avoid the loss of Li due to the volatilization of lithium-oxide during the synthesis. The detailed preparation process has been described elsewhere.[36] The A-LLTO powder obtained after annealing at 750 °C was ground and pelletized under the high pressure of 350 MPa. To prevent further Li loss, the powdery pellets were then covered and embedded in the powder of the same composition before sintered at 1350 °C for 6 h to obtain the final product of ceramic pellets. The surface of the A-LLTO ceramic pellets was polished carefully using abrasive papers from #180 to #2000 grade to obtain the thickness of 200 ± 5 μm. A 200 ± 5nm thin interlayer of LiPON was then deposited on one or both sides of the A-LLTO pellets for 2 h at an optimised temperature, particularly 400 °C under N_2 atmosphere with the pressure of 5 mTorr and RF power of 100 W using the RF-sputtering method.

Physical characterization: The microstructural and chemical characterizations of the materials were conducted using an X-ray diffractometer (XRD; D/MAX Ultima III, Rigaku diffractometer with Cu Kα radiation), field emission scanning electron microscope (FE-SEM; Hitachi S-4700), and X-ray photoelectron spectroscopy (XPS; a MultiLab 2000, VG). For clear observation, the surface of the A-LLTO ceramic pellet was heat etched at 1300 °C for 2 h before FE-SEM analysis. The chemical compositions of materials were analysed using inductive coupled plasma atomic emission spectroscopy (ICP-AES; OPTIMA 8300 DV).

The temperature dependence of ionic conductivity of the ceramic pellets was obtained from AC impedance measurements using an impedance analyser (ZIVE SP2) in the frequency range of from 1 Hz to 1 MHz. Prior to the impedance measurement, for good contact with the samples, the samples were coated with a 20 nm-thick platinum thin film on both sides and connected with silver glue before annealing at 500 °C for 1 h. The active area for the impedance measurements was 0.28 cm^2. The testing temperature was controlled to be between 5 and 65 °C. In order to evaluate the stability of A-LLTO ceramics before and after the deposition of LiPON against Li metal electrode, R2032 coin cells with the symmetric configuration of Li/LiPON/A-LLTO/LiPON/Li and Li/A-LLTO/Li were prepared in an argon-filled glove box before impedance measurement in an air atmosphere at 25 °C.

Electrochemical characterization: The LiPON/A-LLTO pellet with 16 mm in diameter was employed in an aprotic type Li-O_2 cell as a solid electrolyte. These modified coin-type Li-O_2 cells were assembled in the argon-filled glove box. The configuration of the Li-O_2 cell is shown in **Fig. S1**. For the Li-O_2 cells, the stainless steel cover of the positive side in the coin cells was drilled to make 17 holes of 1mm diameter, which were evenly distributed to allow the ingress of oxygen gas. A separator of Whatman® glass fibre impregnated with organic electrolyte of 1 M Lithium bis(trifluoromethane sulfonyl)imide (LiTFSI) in tetraethylene glycol dimethyl ether (TEGDME) was placed between the LiPON/A-LLTO pellets and the oxygen electrode to activate the full cell was composed of a Li/LiPON/A-LLTO/Separator/oxygen electrode. Meanwhile, 5 μL of organic electrolyte was inserted between the Li and LiPON/A-LLTO to ensure good surface contact. In this study, carbon and binder free type oxygen electrodes were prepared using the hydrothermal method. Firstly, Ni foam with thickness of 200 μm was rinsed in ethanol ultrasonically, etched in 1 M HCl solution, and rinsed with deionized water. Subsequently, Ni foam was placed into the autoclave, which contained a 500 mL solution blend of 0.02 M $KMnO_4$, 0.01 M $MnSO_4$, and a few drops of NH_3 (28 v.%) solution to maintain the solution pH in the alkaline range. The autoclave was heated to 150 °C and then maintained for 5 h. After cooling to room temperature, the Ni foam was rinsed with deionized water and finally annealed at 450 °C for 5 h. The charge-discharge behaviour of the Li-O_2 cells was investigated using a Wonatech battery cycler. All potential is hereafter reported as indicated potential versus Li/Li^+ potential.

Results and discussion

Structure and electrical characteristics of LiPON/A-LLTO solid electrolyte

Fig. 1a, **1**b, and **1**c show the XRD patterns of A-LLTO powder obtained after annealing at 750 °C, the A-LLTO ceramics pellet obtained after sintering at 1350 °C, and the A-LLTO ceramics pellet coated with LiPON, respectively. All sharp diffraction peaks of both powder and pellet type A-LLTO coincided well with the standard lines of $Li_{0.33}La_{0.56}TiO_3$ (JCPDS card No. 01-087-0935), confirming the perovskite phase with tetragonal crystalline structure and P4/mmm space group. It was observed that no peaks corresponding to the impurity phase were observed. Obviously, owing to the citrate-gel synthesis method, the A-LLTO perovskite phase was prepared successfully at a relatively low temperature of 750 °C, which is reduced by 400 °C from the previously reported annealing temperature of 1150 °C needed to obtain the LLTO phase in the conventional solid state reaction method.[37-39] Remarkably, better crystallinity of perovskite phase was observed for the A-LLTO pellets sintered at 1350 °C compared with the A-LLTO powder. In particular, the peaks with lower intensity corresponding to the planes such as (001), (111), (200), (202), (211), (213) etc. also appeared clearly at high sintering temperature. The lattice parameters of the A-LLTO ceramics sintered at 1350 °C were calculated to be a = 3.87 nm and b = c = 7.74 nm using X'Pert High Score Plus software. In addition, ICP analysis showed that the actual composition of the obtained A-LLTO ceramics pellet was $Li_{0.378}La_{0.562}Ti_{0.99}Al_{0.012}\square_{0.06}O_{3.013}$, where the oxygen content was determined considering the electro-neutrality condition, indicating a negligible deviation between the nominal and actual compositions. After the deposition of the thin LiPON layer, A-LLTO retained the profile of the XRD pattern without the presence of unusual peaks as shown in **Fig. 1**c. This indicates that the deposited LiPON layer is amorphous in nature.

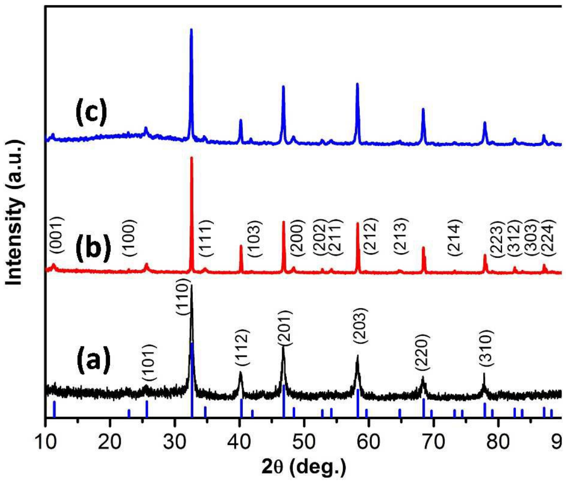

Fig. 1 XRD patterns of (a) A-LLTO powder annealed at 750 °C, (b) A-LLTO pellet obtained after sintering at 1350 °C, and (c) A-LLTO pellet coated with LiPON.

The SEM images of A-LLTO ceramics, shown in **Fig. 2**b indicate that the A-LLTO ceramics sintered at 1350 °C was compact,

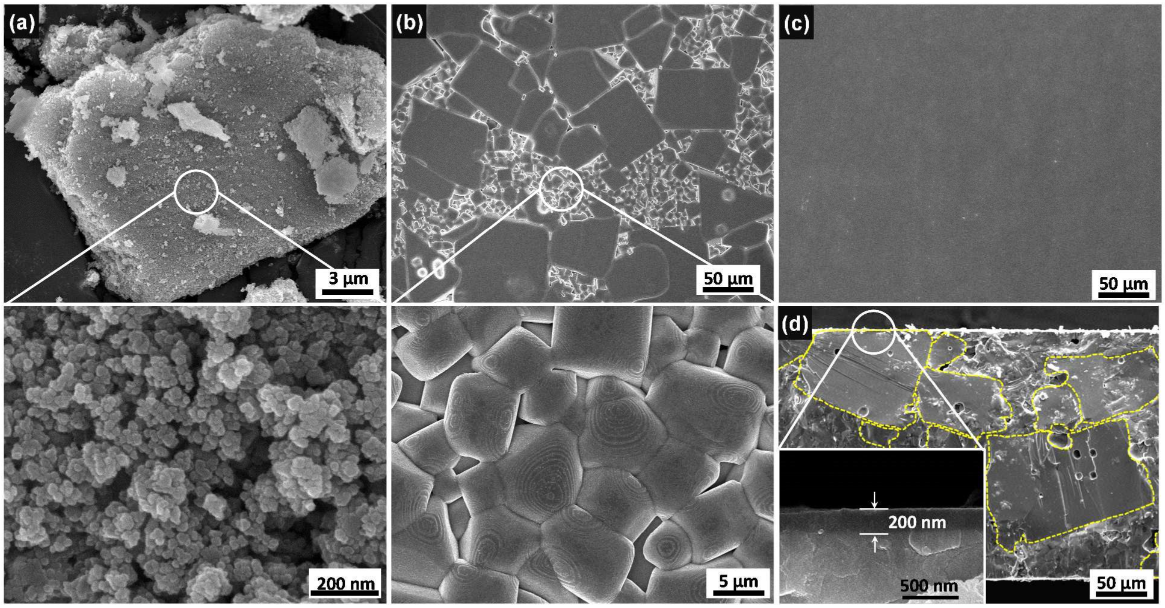

Fig. 2 SEM images of (a) A- LLTO powder annealed at 750 °C, (b) A- LLTO ceramic pellet sintered at 1350 °C, (c) A-LLTO pellet coated with LiPON, and (d) cross section of LiPON/A-LLTO pellet.

and most of the crystallized grains were closely connected. Some grains appeared to have the typical rectangular shape of the tetragonal structure; however, most of them were distorted due to the extremely high pressure in the palletisation process. The large grains with a size ranging from 50 to 100 µm were surrounded by the smaller grains with a grain size ranging from 5 to 10 µm. The grain size found in this study is much larger than that reported for the samples annealed at the same temperature of 1350 °C.[35, 40, 41] In order to understand the reason for this, the morphology of the A-LLTO powder was captured. As seen in **Fig. 2**a, the A-LLTO powder annealed at 750 °C was found to be agglomerates of uniformly fine spherical particles of ~ 50 nm. Accordingly, due to having a high surface area and because of the extremely high pressure in the pelletization process, the A-LLTO powder particles can easily melt and grow into larger grains during the subsequent sintering process at 1350 °C. Besides, the Li is volatile and can easily vaporize from the bulk and grain boundaries of LLTO, which can accelerate the diffusion of the atoms and facilitate the grain growth.[35] Thus, the proper addition of 20 mol.% excess Li_2O (in the form of $LiNO_3$) in stoichiometry contributed to the enhancement of the diffusion rate among particles of the A-LLTO powder to form larger grains. As a result, the grain boundary areas diminished remarkably, which was expected to improve the total ionic conductivity of the A-LLTO.

Fig. 2c shows a SEM surface image of the A-LLTO ceramic pellet coated in a thin LiPON layer using the RF-sputtering method. In comparison with the A-LLTO ceramics before sputtering (**Fig. 2**b), the surface of the LiPON/A-LLTO seems to be smooth, and the grains of A-LLTO were not exposed. This indicates that the entire surface of the A-LLTO pellet was covered with LiPON, which will completely separate the A-LLTO ceramics from the Li metal electrode in the Li-O_2 cell. According to the cross sectional image of the LiPON/A-LLTO sample as shown in **Fig. 2**d, the large grains with a size of ~100 µm in the bulk of the pellet were easily recognized. This image is also similar to the surface image of the A-LLTO pellet observed in **Fig. 2**b. The thickness of the A-LLTO pellet and deposited LiPON were estimated to be 200 µm and 200 nm, respectively. The chemical composition obtained of LiPON was found to be $Li_{3.7}PO_{3.75}N_{0.4}$ from ICP and XPS analysis.

Fig. 3a shows Nyquist impedance plots with a typical blocking electrode response, measured at 25 °C for the A-LLTO pellets with a single LiPON layer (LiPON/A-LLTO) and without LiPON deposition (A-LLTO). By using an equivalent circuit presented in the inset of **Fig. 3**a, the grain, grain boundary, and total conductivity of the samples were evaluated. The grain bulk conductivity was estimated to be 2.99×10^{-3} S cm^{-1}, which is consistent with the previously reported data,[42] while the conductivity of the grain boundary was measured to be 3.55×10^{-4} S cm^{-1}. Accordingly, the total conductivity was calculated to be 3.17×10^{-4} S cm^{-1}, which is a relatively high value among the reported data on the LLTO based ceramics. The high total conductivity obtained for the A-LLTO ceramics after sintering at 1350 °C is mainly attributed to the reduction of resistive grain-boundaries through the grain growth (see **Fig. 2**b). Even after the deposition of LiPON by RF-sputtering, the overall shape of the Nyquist plot for the sample appears to be unchanged. The intercept of the semicircle with the real axis at a higher frequency still represents the bulk resistance. Nevertheless, it reflected the bulk conductivity through both LiPON and A-LLTO. Another intercept determined by the second semicircle at a lower frequency shows the total resistance including the grain boundary of A-LLTO. After fitting the measured data, the total ionic conductivity (σ_{total}) for the LiPON/A-LLTO and LiPON layers was estimated to be 2.25×10^{-4} S cm^{-1} and 7.8×10^{-7} S cm^{-1}, respectively. **Fig. 3**b shows the temperature dependence of the total ionic conductivity of the A-LLTO before and after sputtering LiPON. Interestingly, in the entire measuring temperature range, the conductivity data ($\log\sigma_{total}$) exhibits a typical linear relationship with the reciprocal of the temperature (1/T), which represents an Arrhenius law. Accordingly, the activation energy values were calculated to be 0.36 and 0.41 eV for A-LLTO and LiPON/A-LLTO, respectively. The higher activation energy value obtained for the LiPON/A-LLTO is attributed to the presence of the LiPON layer, which is well known as a low ionic conductivity solid electrolyte.[15, 16, 43]

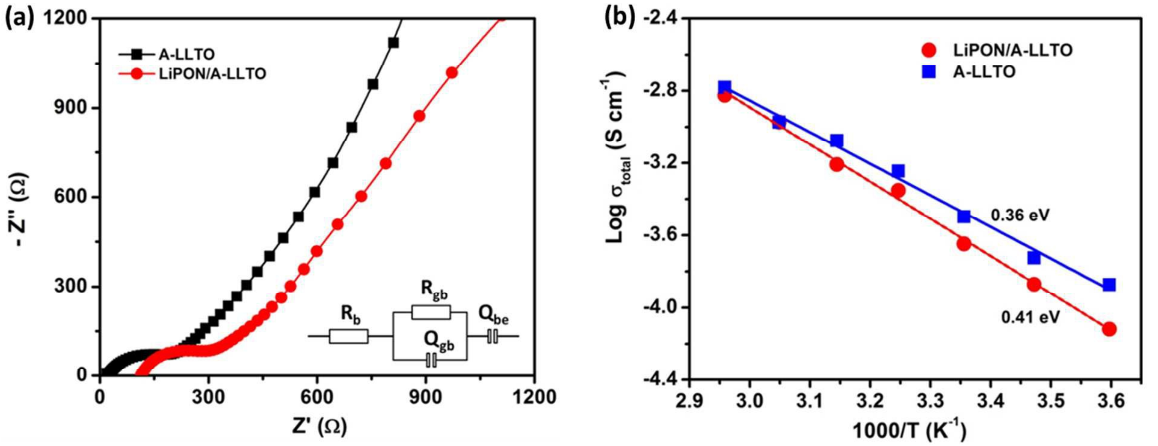

Fig. 3 (a) Nyquist impedance measured at 25 °C and (b) Arrhenius plots for A-LLTO pellets with and without LiPON deposition.

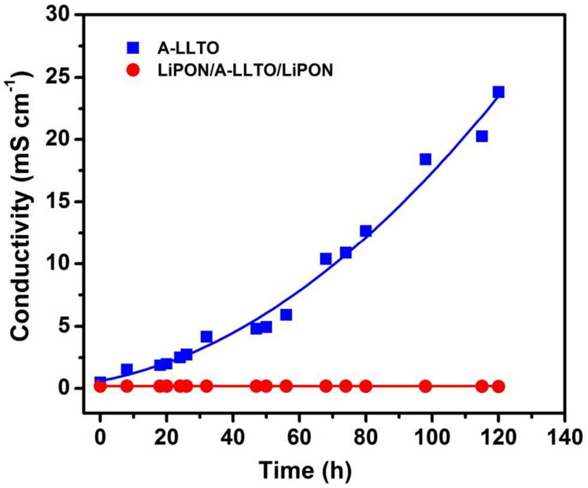

Fig. 4 Variation of conductivity with time for the A-LLTO and LiPON/A-LLTO/LiPON in contact with Li metal on both sides.

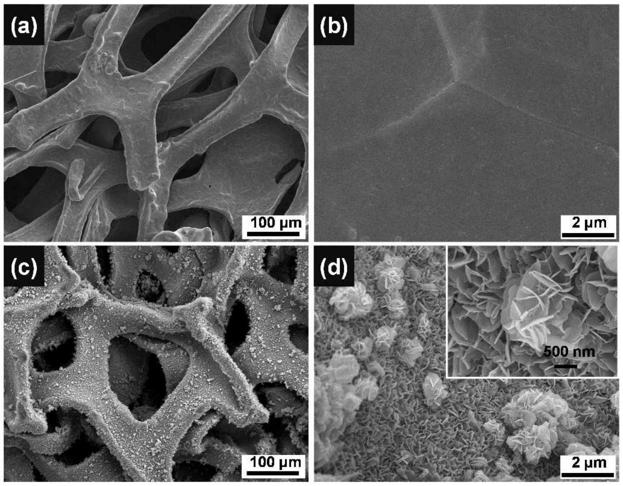

Fig. 5 SEM images of bare Ni foam, (a) low and (b) high magnification. SEM images of MnO_2 nanosheet catalysts formed on Ni foam, (c) low and (d) high magnification.

Fig. 4 shows the stability of the A-LLTO and LiPON/A-LLTO/LiPON samples against the contact with Li metal on both sides of the samples, particularly the total conductivity change of the samples according to storage duration. For the A-LLTO sample, the first impedance measurement of the samples was carried out immediately after assembling the cell, which presented the initial conductivity of 4.66×10^{-4} S cm^{-1}. Subsequently, the total conductivity of the A-LLTO sample in contact with the Li metal dramatically increased with time and reached a conductivity of 2.38×10^{-2} S cm^{-1} after 120 h. This result indicates that A-LLTO is unstable in contact with Li metal, as previously reported in other LLTO ceramics.[28, 41, 44] This is attributed to the reduction of Ti^{4+} to Ti^{3+} by the Li metal as indicated in **Fig. S**2, which leads to an increase in the electronic conductivity, although no structural change was observed (**Fig. S3**a and **S3**b). In contrast, for the LiPON/A-LLTO/LiPON sample, the initial conductivity of 1.75×10^{-4} S cm^{-1} was almost retained during contact with the Li metal up to 120 h. Moreover, as shown in **Fig. S3**c and **S3**d, no unusual phase was observed in the XRD pattern for LiPON/A-LLTO/LiPON, even after direct contact with the Li metal electrode for 120 h. This demonstrates the excellent chemical stability of the LiPON interlayer against the Li metal electrode.

In order to determine the electrochemical stability window for the LiPON deposited A-LLTO, the LiPON/A-LLTO/LiPON sample was polarized between 0 and 5 V. As shown in **Fig. S4**, the current barely passed through the sample, and was nearly zero, demonstrating the good electrochemical stability of the solid electrolytes in the potential range of from 0 to 5 V. Moreover, the LiPON deposited A-LLTO pellet is regarded as a fully electrical insulator in the measured potential window, which can prevent shortening between the anode and cathode when used as a solid electrolyte in batteries including Li-O_2 batteries.

Characterization of carbon-free oxygen electrode

Fig. 5 shows MnO_2 nanosheets (NSs) supported on Ni foam as an oxygen electrode for the Li-O_2 cell. Herein, the MnO_2 nanosheets were deposited on Ni foam using the hydrothermal method and annealed at 450 ^{o}C for 5 h. MnO_2 NSs arrays formed uniformly on the entire surface of the Ni foam as shown in **Fig. 5**c and **5**d. These NSs were interconnected laterally, leading to the formation of a highly open and porous structure, and firmly adhered to the underlying Ni foam (**Fig. 5**a and **5**b). XRD analysis on the NSs confirmed the tetragonal crystalline structure of α-MnO_2 (JCPDS card No. 00-044-0141) as shown in **Fig. S5**. To further analyse the oxide nature of the NSs formed on the surface of the Ni foam, XPS analysis was also carried out. The XPS spectra (**Fig. S6**) exhibited the sharp peak position of 641.8 eV corresponding to Mn $2p_{3/2}$ and the magnitude of peak splitting of 4.9 eV corresponding to Mn 3s, suggesting that the oxidation state of Mn is ~ 4. This also demonstrates that the NSs were primarily composed of MnO_2, which is in good agreement with the obtained XRD results as well as the previously reported references.[45, 46]

Electrochemical characteristics of the cells employing LiPON/A-LLTO solid electrolyte

To investigate the electrochemical performance of LiPON/A-LLTO, the symmetric cells composed of Li/LiPON/A-LLTO/LiPON/Li were assembled in a R2032 type coin cell. **Fig. 6**a shows the cell potential profile at 1 h intervals under different applied charge-discharge currents varying from 0.1 to 1 mA and corresponding to the current density for Li metal plating and stripping from 0.05 to 0.5 mA cm^{-2}. When the charge-discharge current was lower than 0.6 mA, the potential profile of the symmetric cell retained its typical symmetric shape; no increase in overpotential with time for each step was observed. In contrast, when the charge-discharge current exceeded 0.6 mA, the symmetric cell exhibited high overpotential which increased gradually with time. Accordingly, the current density of 0.3 mA cm^{-2} was safely determined as a limiting current density for the further testing of the Li-O_2 cell employing the LiPON/A-LLTO electrolyte.

Further, the Li-O_2 cell employing the carbon-free MnO_2 catalyst based oxygen electrode and the Li metal electrode protected by the LiPON/A-LLTO layers was galvanostatically cycled within the cell potential range of from 2.0 to 4.5 V in variety of the applied current densities ranging from 0.05 to 0.5 mA cm^{-2}. **Fig. 6**b shows the 1st discharge-charge potential profiles of the Li-O_2 cell. Normally, the potential gap (ΔE) between the discharge and charge potentials can provide information on the degree of cell polarization in both the discharge and charge processes. As seen, at the low charge-discharge rates of from 0.05 to 0.3 mA cm^{-2}, the average discharge potential of the cell decreased from 2.53 V to 2.07 V and the corresponding ΔE increased from 1.52 V to 2.02 V with increase in applied current density. Meanwhile, at the high charge-discharge rates of more than 0.3 mA cm^{-2}, similar to the result for the symmetric cell, the discharge curve for the Li-O_2 cell no longer retained the potential plateau. Simultaneously, the capacity of the cell also degraded rapidly. The highest specific capacity achieved for the Li-O_2 cell was 10045 mA h g^{-1} under the current density of 0.05 mA cm^{-2}.

In order to investigate the influence of LiPON/A-LLTO on the charge-discharge cyclability of the cell, the Li-O_2 cell using a pristine Li metal anode without the protection of LiPON/A-LLTO was fabricated for comparison. **Fig. 6**c displays the 1st discharge and charge profiles for the Li-O_2 cells with and without LiPON/A-LLTO under the applied current density of 0.1 mA cm^{-2}. For the cell employing LiPON/A-LLTO as a protective solid electrolyte layer for the Li electrode, the initial average discharge and charge potentials were ~2.51 V and ~4.09 V, respectively. In addition, the measured specific discharge capacity for the cell was 8925 mA h g^{-1}. The degree of polarization for discharge-charge (ΔE) in the cell with LiPON/A-LLTO was found to be 1.58 V. In contrast, for the Li-O_2 cell without LiPON/A-LLTO, the ΔE was smaller and was estimated to be 1.49 V, with the initial average discharge potential of 2.57 V and the subsequent average charge potential of 4.06 V. However, the protection of the Li metal from oxygen gas and/or contaminants diffusing from the cathode as well as the

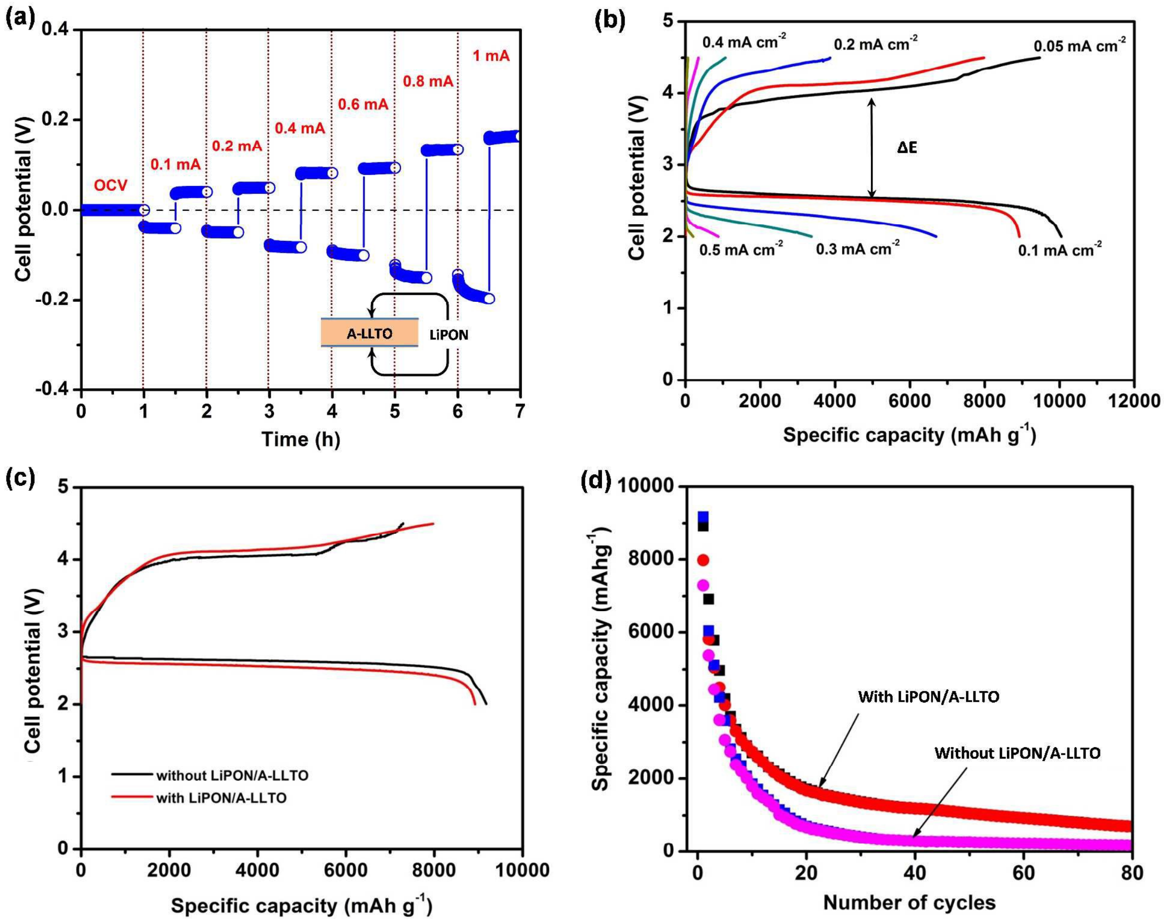

Fig. 6 (a) Charge-discharge potential profile with time for the symmetric cell of Li/LiPON/A-LLTO/LiPON/Li, measured by varying applied current; (b) 1st charge-discharge profile for Li-O_2 cell employing LiPON/A-LLTO at various current densities ranging from 0.05 to 0.5 mA cm^{-2}; (c) 1st charge-discharge profile for Li-O_2 cell with and without LiPON/A-LLTO, measured at the potential range of 2.0-4.5 V under the applied current density of 0.1 mA cm^{-2} and (d) the corresponding cyclability.

prevention of the dendritic growth of the Li metal can be expected, although the Li-O_2 cell with LiPON/A-LLTO exhibited a larger initial internal resistance resulting in higher initial polarization. Accordingly, the cell with LiPON/A-LLTO exhibited a predominant cyclability over the cell without LiPON/A-LLTO as shown in **Fig. 6**d. After 80 cycles in the cycling test, the Li-O_2 cell with LiPON/A-LLTO remained at a specific capacity greater than 500 mA h g^{-1}, while the Li-O_2 cell without LiPON/A-LLTO delivered only the capacity of 175 mA h g^{-1}.

To further clarify the improvement of the cycleability of the Li-O_2 cell employing the LiPON/A-LLTO, the Li-O_2 cell was galvanostatically cycled at 0.1 mA cm^{-2} under the limited capacity mode of 1000 mA h g^{-1} within the cut-off potential range between 2.0 V and 4.5V as shown in **Fig. 7**. As expected, the end cell potential of the Li-O_2 cell, in which the Li metal electrode was protected by LiPON/A-LLTO, gradually decayed within the first 90 cycles and then rapidly faded from the 91st cycle onward (**Fig. 7**a). From the 129th cycle, the discharge cell potential dropped to 2.0 V before reaching the capacity limit of 1000 mA h g^{-1}. At the cut-off cell potential of 2.0 V, the cell only achieved the capacity of 872 mA h g^{-1} (**Fig. 7**c). In contrast, for the cell containing the pristine Li metal electrode, the discharge specific capacity of 1000 mA h g^{-1} was maintained only for 47 cycles (**Fig. 7**b). In the 48th cycle, before falling to the cut-off potential of 2.0 V, the cell attained the discharge capacity of 705 mA h g^{-1} (**Fig. 7**d).

The protectiveness of LiPON/A-LLTO for the Li metal electrode can be further identified using electrochemical impedance spectroscopy (EIS). **Fig. 8**a shows the impedance spectra for the Li-O_2 cells before and after charge-discharge tests under the limited capacity mode. On the whole, the shape of the Nyquist plots for the Li-O_2 cell with and without LiPON/A-LLTO appeared to be similar. However, before the test, the impedance of the Li-O_2 cell with LiPON/A-LLTO was larger than that of the cell without LiPON/A-LLTO due to the contribution of the interfacial resistance of the LiPON/A-LLTO solid electrolyte in the complex impedance of the cell. Accordingly, the total degree of polarization, which was expressed as *ΔE*, was larger in the 1st cycle of the cell with LiPON/A-LLTO than that of the cell without LiPON/A-LLTO (**Fig. 6**c). Interestingly, after 129 cycles and 48 cycles of charge-discharge under the limited capacity mode of 1000 mA h g^{-1}, the impedance spectra exhibited a negligible difference between the cells with and without LiPON/A-LLTO.

During the charge-discharge cycling of the Li-O_2 cell, resistive Li_2O_2 and other products formed on the surface of the oxygen

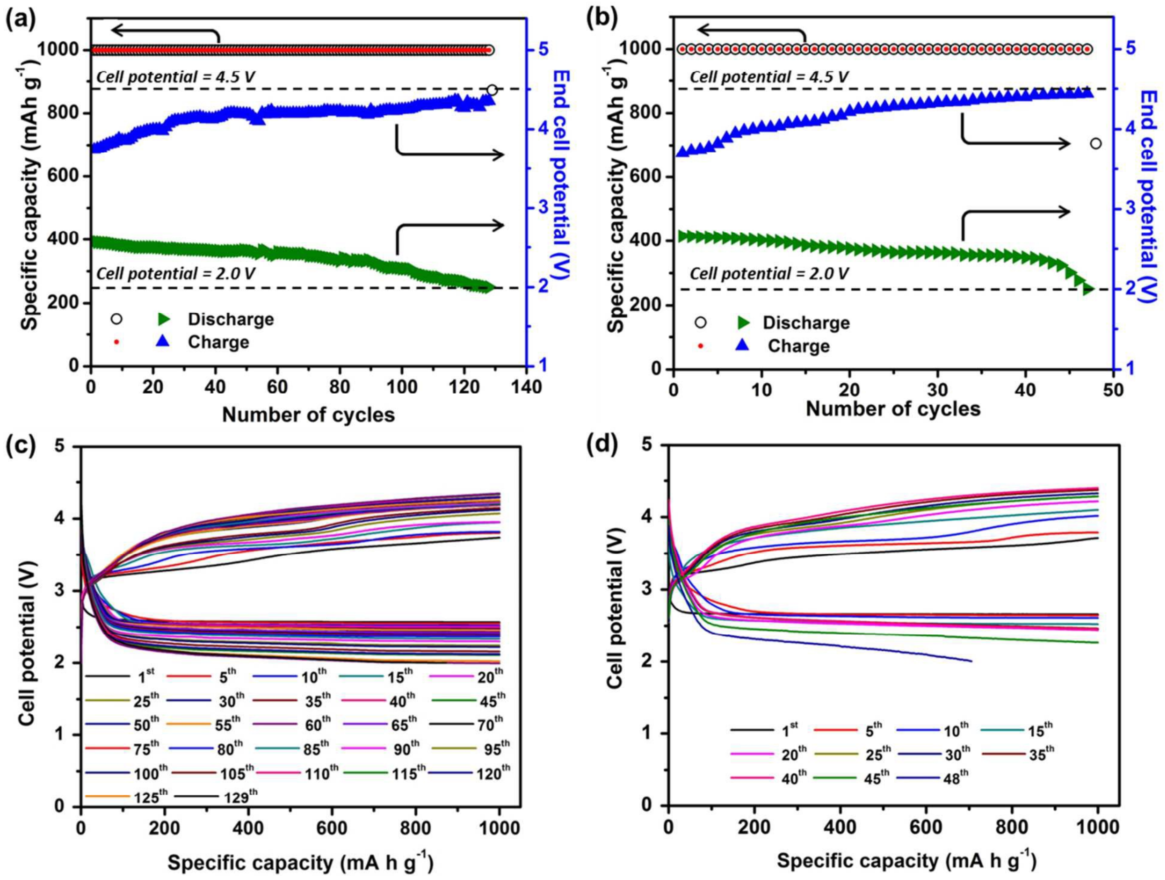

Fig. 7 Variation of end cell potential with cycle for the Li-O_2 cells (a) with and (b) without LiPON/A-LLTO, tested under limited capacity mode of 1000 mA h g^{-1}; the corresponding charge-discharge curves for the Li-O_2 cells (c) with and (d) without LiPON/A-LLTO.

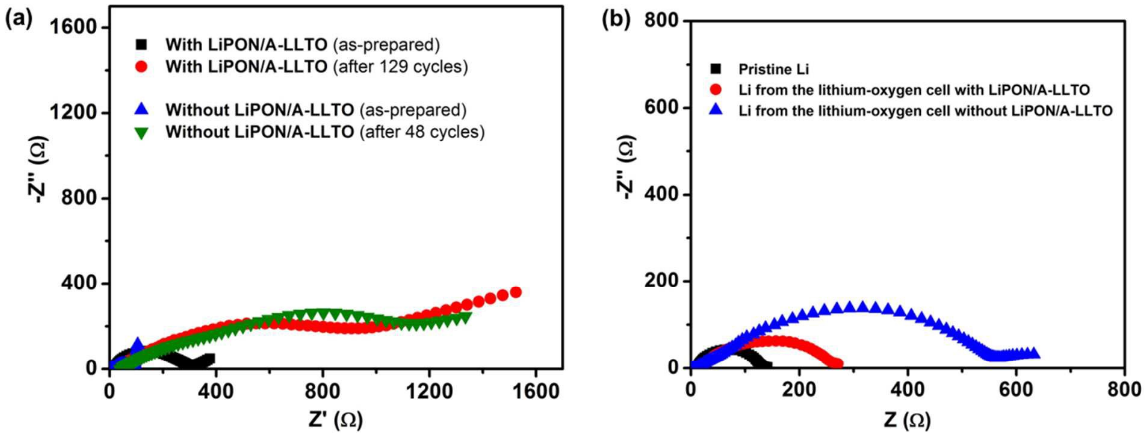

Fig. 8 (a) Impedance spectra for the lithium-oxygen cell with LiPON/A-LLTO as-prepared and after charge-discharge test under limited capacity mode for 129 cycles and for the lithium-oxygen cell without LiPON/A-LLTO as-prepared and after 48 charge-discharge cycles, respectively. (b) Impedance spectra for the symmetric cells composed of (fresh Li/separator/pristine or tested Li), where the Li electrode had been cyclic tested under the limited capacity mode and extracted from the cells shown in (a).

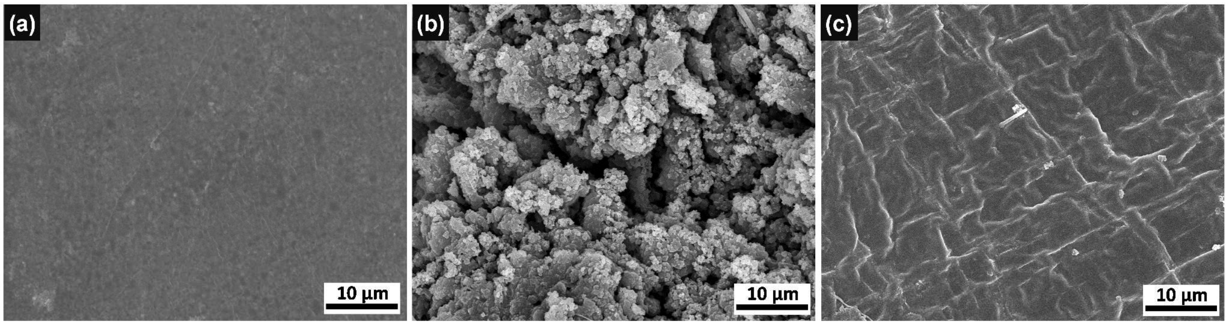

Fig. 9 SEM images of the surface of (a) pristine Li metal electrode and Li metal electrodes; (b) without the protection of LiPON/A-LLTO after cyclic charge-discharge test for 48 cycles; and (c) with protection by LiPON/A-LLTO after test for 129 cycles, under a limited capacity mode of 1000 mA h g^{-1}.

electrode as shown in **Fig. S7-9**, which strongly concurs with the previous literature,[47, 48] leading to an increase in impedance of the cell.[49] Therefore, to investigate the independent effect of the deterioration of Li electrode on the degradation of the full cell, the Li electrodes after cycling under limited capacity mode were detached from the Li-O_2 cells in an argon filled glove-box and reassembled into new symmetric cells with configurations such as (fresh Li/Separator/tested Li), where the separator was impregnated with the new electrolyte of 1 M LiTFSI in TEGDME. Another symmetric cell composed of (fresh Li/Separator /fresh Li) was also prepared for comparison. As shown in **Fig. 8**b, the impedance of the symmetric cell of (fresh Li/Separator /tested Li) was found to increase compared to that for the symmetric cell of (fresh Li/Separator/fresh Li) due to the change in the surface during charge-discharge. In particular, the interfacial resistance, which includes the contributions from the charge transfer resistance and the Li ion transport resistance through the passivation layers, increased after the test. Remarkably, the Li electrode without the protectiveness of LiPON/A-LLTO showed a significantly larger interfacial resistance than that for the Li electrode protected by LiPON/A-LLTO in the Li-O_2 cell. Electrochemically, this demonstrates that the degradation of the Li electrode in the cell without A-LLTO is the major contribution to the deterioration of the full Li-O_2 cell.

Generally, the change in interfacial resistance of the Li metal electrode is closely related to the change in its own morphology and surface chemistry.[21, 50, 51] To investigate the effect of LiPON/A-LLTO on the change in the surface morphology of the Li metal surface after cycling, the surface of the tested Li electrodes was observed using the SEM micrographs. As can be seen in **Fig. 9**a, the pristine Li metal electrode exhibited a smooth flat surface. However, after charge-discharge cycling, the surface morphology of the Li metal electrode changed dramatically. The unprotected Li electrode without LiPON/A-LLTO revealed the typical mossy surface of the dendrite (**Fig. 9**b), while the Li electrode protected by LiPON/A-LLTO still maintained a relatively

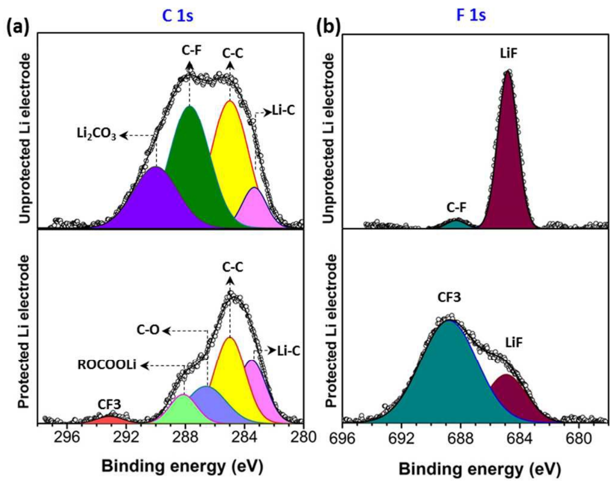

Fig. 10 (a) C1s and (b) F1s XPS spectra of unprotected Li electrode by LiPON/A-LLTO after cyclic discharge-charge test for 48 cycles (top) and protected Li electrode by LiPON/A-LLTO after test for 129 cycles (bottom), under limited capacity mode of 1000 mA h g^{-1}.

smooth surface (**Fig. 9**c). Therefore, by employing the LiPON/A-LLTO solid electrolyte, any corrosion of the Li metal electrode is avoided and the growth of the lithium dendrites is completely suppressed by the mechanical strength. Thus, the uniformity of Li deposition and dissolution during the charge-discharge process of the Li-O_2 cell was ensured, and the dense smooth surface of the protected Li electrode was still maintained, similar to the pristine Li electrode. Accordingly, the surface resistance of the Li electrode can be retained stably by avoiding the electrolyte deposition at the new Li surface. This explains why the impedance measured for the protected Li electrode was much smaller than that for the unprotected Li electrode.

Subsequently, to determine the role of LiPON/A-LLTO in preventing the diffusion of oxygen and other contaminants through the liquid electrolyte to react with the Li metal electrode in the Li-O_2 cell, the surface chemistries of the Li electrode with and without the protectiveness of LiPON/A-LLTO after cycling were also analysed using XPS. As shown in **Fig. 10**a, in the high-resolution C1s spectra of both electrodes, the Li electrode protected by LiPON/A-LLTO showed five peaks at binding energies of 283.5, 285, 286.6, 288.1, and 293 eV, which correspond to alkyl lithium (Li-C), hydrocarbon (C-C), ethers (C-O), lithium alkylcarboxylate (ROCOOLi), and carbon flourine (-CF_3), respectively, representing the characteristics of the passivation layer from the 1 M LiTFSI TEGDME electrolyte.[21, 52-54] In contrast, for the unprotected Li electrode without LiPON/A-LLTO, only two of the four peaks corresponding to alkyl lithium and hydrocarbon were found to be similar to that of the protected Li electrode. Two remaining peaks were found at 290 eV corresponding to lithium carbonate (Li_2CO_3), which is normally formed via the reductive decomposition of cyclic carbonate-based electrolytes,[55-57] while another peak was found at 287.7 eV, which was referred to as the C-F bond species, suggesting the deeper decomposition of the ethereal solvent and LiTFSI salt.[58] In other words, the F 1s spectra of both the protected and unprotected Li electrodes (**Fig. 10**b) show the presence of LiF at low binding energy (684.9 eV). This LiF has originated from the decomposition of the LiTFSI salt, which contains F. It should be noted that, the contribution of the LiF peak into the F 1s spectra of the unprotected Li electrode was much greater than that of the protected Li electrode. This demonstrates that the SEI layer of the unprotected Li electrode was constructed by a large amount of the LiF decomposition product. As previously reported, when the surface films are comprised of LiF as a major component, they are highly resistive.[59] This is also the reason why the unprotected Li electrode showed the high impedance in comparison with the protected Li electrode (see **Fig. 8**b). Apparently, all obtained XPS results revealed a much more violent electrolyte decomposition degree (including the ethereal solvent and LiTFSI salt) on the surface of the Li electrode in the Li-O_2 cell without the protectiveness of the LiPON/A-LLTO solid electrolyte. This can be attributed to the presence of oxygen diffusing from the cathode side, which possibly caused violent reactions with the new Li generated in the charge process or catalysed the electrolyte decomposition reactions occurring on the surface of the Li electrode during the operation of the Li-O_2 cell.[60, 61] Due to the presence of LiPON/A-LLTO, the transportation of oxygen and other contaminants from the cathode through the liquid electrolyte was completely prevented. Accordingly, the electrolyte in the Li-O_2 cell was less decomposed, resulting in the improvement in the long-term cyclability for the Li-O_2 using LiPON/A-LLTO.

To further evaluate the stability of LiPON/A-LLTO after the cyclic charge-discharge test, the total conductivity of LiPON/A-LLTO after the cycling test for 129 cycles was examined and found to suffer a slight decrease to 1.65×10^{-4} S cm^{-1}. Meanwhile, negligible changes in the structure and morphology of LiPON/A-LLTO before and after charge-discharge cycling test were observed as shown in **Fig. S10** and **Fig. S11**, respectively. Further, XPS analysis of the LiPON surface in LiPON/A-LLTO did not indicate any position shift for

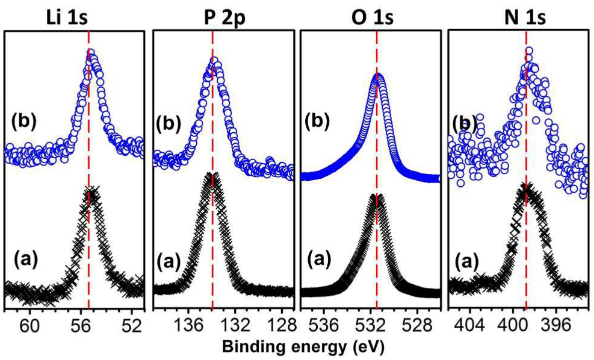

Fig. 11 XPS spectra of Li 1s, P 2p, O 1s, and N 1s corresponding to LiPON surface in the LiPON/A-LLTO pellets from the Li-O_2 cells (a) before and (b) after test for 129 cycles under the limited capacity mode of 1000 mA h g^{-1}.

the core peak of Li 1s, P 2p, O 1s, and N 1s even after the cycling test (**Fig. 11**). This demonstrates that the chemical composition of LiPON remained dynamically stable even after contact with the Li metal electrode during the cycling process.[62]

Conclusions

In the present study, the LiPON/A-LLTO was successfully employed as a solid electrolyte in the non-aqueous Li-O_2 cell. The Li-O_2 cell containing the Li metal electrode protected by LiPON/A-LLTO exhibited significantly enhanced cycling stability with the cycle life of 128 cycles under the limited capacity mode of 1000 mA h g^{-1} within the potential range of from 2.0 to 4.5 V compared with the cell without LiPON/A-LLTO exhibiting the cycle life of 47 cycles. Impedance, SEM, and XPS analyses confirmed that the improved cycle life of the Li-O_2 cell using the protected Li metal electrode with LiPON/A-LLTO resulted from the effective suppression of lithium dendrite growth by the mechanical strength, as well as the suppression of electrolyte decomposition due to the prevention of the diffusion of oxygen and other contaminants from the oxygen electrode side during the operation of the Li-O_2 cell.

Acknowledgement

This work was supported by the Ministry of Trade, Industry & Energy (MOTIE), Korea, under the Energy Efficiency & Resources Core Technology Program of the Korea Institute of Energy Technology Evaluation and Planning (KETEP) (No. 20112020100110/KIER B4-2462), and by the Ministry of Education, Korea under Basic Science Research Program of the National Research Foundation of Korea (NRF) (No. 2015R1D1A3A01019399).

Notes and references

‡ Footnotes relating to the main text should appear here. These might include comments relevant to but not central to the matter under discussion, limited experimental and spectral data, and crystallographic data.

1. Q.-C. Liu, J.-J. Xu, D. Xu and X.-B. Zhang, Nat. Commun., 2015, 6.
2. J.-J. Xu, D. Xu, Z.-L. Wang, H.-G. Wang, L.-L. Zhang and X.-B. Zhang, Angew. Chem. Int. Ed., 2013, 52, 3887-3890.
3. L. Li, S.-H. Chai, S. Dai and A. Manthiram, Energy Environ. Sci., 2014, 7, 2630-2636.
4. Z.-L. Wang, D. Xu, J.-J. Xu and X.-B. Zhang, *Chem. Soc. Rev.*, 2014, **43**, 7746-7786.
5. P. He, Y. Wang and H. Zhou, Electrochem. Commun., 2010, 12, 1686-1689.
6. H.-G. Jung, J. Hassoun, J.-B. Park, Y.-K. Sun and B. Scrosati, *Nat. Chem.,* 2012, **4**, 579-585.
7. H.-D. Lim, K.-Y. Park, H. Gwon, J. Hong, H. Kim and K. Kang, *Chem. Commun.*, 2012, **48**, 8374-8376.
8. J.-J. Xu, Z.-L. Wang, D. Xu, L.-L. Zhang and X.-B. Zhang, *Nat. Commun.*, 2013, **4**, 2438.
9. J.-J. Xu, Z.-L. Wang, D. Xu, F.-Z. Meng and X.-B. Zhang, *Energy Environ. Sci.*, 2014, **7**, 2213-2219.
10. T. Zhang and H. Zhou, *Nat. Commun.*, 2013, **4**, 1817.
11. M. S. Park, S. B. Ma, D. J. Lee, D. Im, S.-G. Doo and O. Yamamoto, *Sci. Rep.*, 2014, **4**, 3815.
12. Z. Li, J. Huang, B. Yann Liaw, V. Metzler and J. Zhang, *J. Power Sources*, 2014, **254**, 168-182.
13. K. Nishikawa, T. Mori, T. Nishida, Y. Fukunaka, M. Rosso and T. Homma, *J. Electrochem. Soc.*, 2010, **157**, A1212-A1217.
14. G. Zheng, S. W. Lee, Z. Liang, H.-W. Lee, K. Yan, H. Yao, H. Wang, W. Li, S. Chu and Y. Cui, *Nat. Nano.*, 2014, **9**, 618-623.
15. Y. Sun, *Nano Energy*, 2013, **2**, 801-816.
16. J. W. Fergus, *J. Power Sources*, 2010, **195**, 4554-4569.
17. M. C. López, G. F. Ortiz, E. M. Arroyo-de Dompablo and J. L. Tirado, *Inorg. Chem.*, 2014, **53**, 2310-2316.
18. L. Cheng, J. S. Park, H. Hou, V. Zorba, G. Chen, T. Richardson, J. Cabana, R. Russo and M. Doeff, *J. Mater. Chem. A*, 2014, **2**, 172-181.
19. Y. Zhu, S. Xiao, Y. Shi, Y. Yang and Y. Wu, *J. Mater. Chem. A*, 2013, **1**, 7790-7797.
20. R.-J. Chen, M. Huang, W.-Z. Huang, Y. Shen, Y.-H. Lin and C.-W. Nan, *J. Mater. Chem. A*, 2014, **2**, 13277-13282.
21. D. J. Lee, H. Lee, J. Song, M.-H. Ryou, Y. M. Lee, H.-T. Kim and J.-K. Park, *Electrochem. Commun.*, 2014, **40**, 45-48.
22. S. J. Kang, T. Mori, J. Suk, D. W. Kim, Y. Kang, W. Wilcke and H.-C. Kim, *J. Mater. Chem. A*, 2014, **2**, 9970-9974.
23. T. T. Truong, Y. Qin, Y. Ren, Z. Chen, M. K. Chan, J. P. Greeley, K. Amine and Y. Sun, *Adv. Mater.*, 2011, **23**, 4947-4952.
24. Y. Wang and H. Zhou, *Energy Environ. Sci.*, 2011, **4**, 1704-1707.
25. T. Zhang, N. Imanishi, S. Hasegawa, A. Hirano, J. Xie, Y. Takeda, O. Yamamoto and N. Sammes, *J. Electrochem. Soc.*, 2008, **155**, A965-A969.
26. H. He, W. Niu, N. M. Asl, J. Salim, R. Chen and Y. Kim, *Electrochim. Acta*, 2012, **67**, 87-94.
27. L. Li, X. Zhao, Y. Fu and A. Manthiram, *Phys. Chem. Chem. Phys.*, 2012, **14**, 12737-12740.
28. Y. Inaguma, C. Liquan, M. Itoh, T. Nakamura, T. Uchida, H. Ikuta and M. Wakihara, *Solid State Commun.*, 1993, **86**, 689-693.
29. Y. Harada, T. Ishigaki, H. Kawai and J. Kuwano, *Solid State Ionics*, 1998, **108**, 407-413.
30. S. Stramare, V. Thangadurai and W. Weppner, *Chem. Mater.*, 2003, **15**, 3974-3990.
31. O. Bohnke, C. Bohnke and J. L. Fourquet, *Solid State Ionics*, 1996, **91**, 21-31.
32. O. Bohnke, Q. N. Pham, A. Boulant, J. Emery, T. Šalkus and M. Barré, *Solid State Ionics*, 2011, **188**, 144-147.
33. K. Chen, M. Huang, Y. Shen, Y. Lin and C. W. Nan, *Solid State Ionics*, 2013, **235**, 8-13.
34. Y. Inaguma and M. Nakashima, *J. Power Sources*, 2013, **228**, 250-255.
35. H. Geng, J. Lan, A. Mei, Y. Lin and C. W. Nan, *Electrochim. Acta*, 2011, **56**, 3406-3414.
36. H. T. T. Le, R. S. Kalubarme, D. T. Ngo, S.-Y. Jang, K.-N. Jung, K.-H. Shin and C.-J. Park, *J. Power Sources*, 2015, **274**, 1188-1199.
37. J. Emery, J. Y. Buzare, O. Bohnke and J. L. Fourquet, *Solid State Ionics*, 1997, **99**, 41-51.

38. Y. Inaguma, L. Chen, M. Itoh and T. Nakamura, *Solid State Ionics*, 1994, **70–71, Part 1**, 196-202.
39. Q. N. Pham, C. Bohnke and O. Bohnke, *Surf. Sci.*, 2004, **572**, 375-384.
40. K. Chen, M. Huang, Y. Shen, Y. Lin and C. W. Nan, *Electrochim. Acta*, 2012, **80**, 133-139.
41. K. Chen, M. Huang, Y. Shen, Y. Lin and C. W. Nan, *Solid State Ionics*, 2013, **235**, 8-13.
42. A. Morata-Orrantia, S. García-Martín and M. Á. Alario-Franco, *Chem. Mater.*, 2003, **15**, 3991-3995.
43. W. C. West, J. F. Whitacre and J. R. Lim, *J. Power Sources*, 2004, **126**, 134-138.
44. P. Knauth, *Solid State Ionics*, 2009, **180**, 911-916.
45. M. Kundu, C. C. A. Ng, D. Y. Petrovykh and L. Liu, *Chem. Commun.*, 2013, **49**, 8459-8461.
46. L. Zhang, F. Zhang, G. Huang, J. Wang, X. Du, Y. Qin and L. Wang, *J. Power Sources*, 2014, **261**, 311-316.
47. K. P. C. Yao, D. G. Kwabi, R. A. Quinlan, A. N. Mansour, A. Grimaud, Y.-L. Lee, Y.-C. Lu and Y. Shao-Horn, *J. Electrochem. Soc.*, 2013, **160**, A824-A831.
48. Y. Qin, J. Lu, P. Du, Z. Chen, Y. Ren, T. Wu, J. T. Miller, J. Wen, D. J. Miller, Z. Zhang and K. Amine, *Energy Environ. Sci.*, 2013, **6**, 519-531.
49. R. S. Kalubarme, G.-E. Park, K.-N. Jung, K.-H. Shin, W.-H. Ryu and C.-J. Park, *J. Electrochem. Soc.*, 2014, **161**, A880-A889.
50. G. Ma, Z. Wen, Q. Wang, C. Shen, J. Jin and X. Wu, *J. Mater. Chem. A*, 2014, **2**, 19355-19359.
51. G. Ma, Z. Wen, M. Wu, C. Shen, Q. Wang, J. Jin and X. Wu, *Chem. Commun.*, 2014, **50**, 14209-14212.
52. H. Lee, D. J. Lee, Y.-J. Kim, J.-K. Park and H.-T. Kim, *J. Power Sources*, 2015, **284**, 103-108.
53. A. Schechter, D. Aurbach and H. Cohen, *Langmuir*, 1999, **15**, 3334-3342.
54. W. Li, H. Yao, K. Yan, G. Zheng, Z. Liang, Y.-M. Chiang and Y. Cui, *Nat. Commun.*, 2015, **6,** 7436.
55. R. Dedryvère, L. Gireaud, S. Grugeon, S. Laruelle, J. M. Tarascon and D. Gonbeau, *J. Phys. Chem. B*, 2005, **109**, 15868-15875.
56. D. Aurbach, Y. Ein-Ely and A. Zaban, *J. Electrochem. Soc.*, 1994, **141**, L1-L3.
57. S. A. Freunberger, Y. Chen, Z. Peng, J. M. Griffin, L. J. Hardwick, F. Bardé, P. Novák and P. G. Bruce, *J. Am. Chem. Soc.*, 2011, **133**, 8040-8047.
58. D. Aurbach, A. Zaban, Y. Ein-Eli, I. Weissman, O. Chusid, B. Markovsky, M. Levi, E. Levi, A. Schechter and E. Granot, *J. Power Sources*, 1997, **68**, 91-98.
59. D. Aurbach, *J. Power Sources*, 2000, **89**, 206-218.
60. R. Younesi, M. Hahlin, M. Roberts and K. Edström, *J. Power Sources*, 2013, **225**, 40-45.
61. S. A. Freunberger, Y. Chen, N. E. Drewett, L. J. Hardwick, F. Bardé and P. G. Bruce, *Angew. Chem. Int. Ed.*, 2011, **50**, 8609-8613.
62. B. Fleutot, B. Pecquenard, H. Martinez and A. Levasseur, *Solid State Ionics*, 2012, **206**, 72-77.

Graphical abstract

Bi-layer lithium phosphorous oxynitride/aluminium substituted lithium lanthanum titanate as promising solid electrolyte for long-life rechargeable lithium-oxygen batteries

Hang T.T. Le, Ramchandra S. Kalubarme, Duc Tung Ngo, Harsharaj S. Jadhav, and Chan- Jin Park*